THE JOURNAL OF CHEMICAL PHYSICS **134**, 194108 (2011)

Global minimum structures and structural phase diagrams of modified Morse clusters: 11 ≤ *N* ≤ 30

Jing Wu and Longjiu Cheng[a)]
School of Chemistry and Chemical Engineering, Anhui University, Hefei, Anhui 230039, People's Republic of China

(Received 17 November 2010; accepted 6 April 2011; published online 18 May 2011)

The energetically favored structures of clusters are determined by the interactions among particles. Using the modified Morse pair potential, which has two parameters that can freely control the interactions at the minimum, short range, and long range, we systematically investigated how the interactions determines the global minimum structures of clusters and gave the structural phase diagram at 0 K for each cluster size at the range $11 \leq N \leq 30$. Compared to the Morse potential, a number of new structures are found, and some of them are unexpected. The global minimum structures of modified Morse clusters can act as structural bank, which will be helpful in the optimization of certain real clusters. © *2011 American Institute of Physics*. [doi:10.1063/1.3582790]

I. INTRODUCTION

Global optimization of clusters is of great importance for chemical and physical science. Compared to bulk materials, the study on global minima of clusters is always novel and lots of global minima have been located.[1–9] Wales group built the Cambridge Cluster Database[10] by a systematic research on potential energy surface (PES).[3,11,12]

Generally, a quantum mechanics method is much expensive for global geometric optimization. Also, many empirical potentials are too complicated to get a physical insight into the observed structures. So the simple models are usually used to fit the interatomic potentials for various clusters such as Lennard-Jones (LJ) (Ref. 13) and Morse[14] potentials. For LJ potential, only the van der waals's force is considered. LJ potential can be successfully applied to some real systems such as heavy inert gas atoms at low temperature. And more frequently, it is a popular benchmark for new theoretical methods. The global minima of small LJ clusters are icosahedral, then with clusters size increasing, decahedral become favored, and finally, close-packed motifs become predominant.[10]

Morse function has one parameter that can control the range of the potential. For short-ranged Morse clusters, icosahedral structures are so strained that decahedral and strain-free close-packed structures become predominant, but for long-ranged Morse clusters, disordered and polyicosahedral[15,16] structures are predominant. Doye *et al.*[17,18] have made a systematic search of the putative global minimum structures for clusters size $N \leq 80$ by Morse potential as a function of the range of the potential. Later on, the structures of Morse clusters at $81 \leq N \leq 240$ were also modeled and the structural phase diagram was given out.[19,20]

For Morse function, potential ranges at the short and long distance change with the parameter at the same time. So we designed a modified model (MM) potential[21] based on the Morse potential to get a systematic study about the effect of long and short range interactions. It can freely control the interaction at the minimum, short range, and long range of the potential. However, there is still no systematic study on how the range of the potential affects the global minimum structures by using the MM potential. For this purpose, in this work, we try to locate the putative global minimum structures of MM cluster as the function of potential range.

For $N \leq 10$, the putative global minimum structures of Morse clusters have been located,[17] and the effects of potential range are not so large at small cluster size. Therefore, we start our work at $11 \leq N \leq 30$. A number of new motifs are found to be global minimum at certain potential range, and the structural phase diagram at each cluster size is carried out.

For real clusters (such as metal clusters, nanoalloy clusters, and molecular clusters), the interaction mechanism among particles is often very complicated, and the energetically favored motifs may also be unexpected. However, for some of the real cases, the interactions may be similar to the modified Morse potential at certain potential range (minimum, long distance, and short distance of the potential). Therefore, the structural phase diagrams of the modified Morse clusters can act as a structural bank, and the global minimum motifs can be the starting points of first principle calculations.

II. COMPUTATIONAL METHODS

A. The modified Morse model potential

The MM potential designed based on Morse potential can be written as

$$\begin{aligned}\mathrm{MM}[\rho,\varphi](r) = (&\exp[2\rho(1-r^{\varphi})/\varphi]\\ &-2\exp[\rho(1-r^{\varphi})/\varphi]-A)\,/(1+A),\end{aligned} \tag{1}$$

where r is the pair distance;[22] ρ and φ are two parameters, $A = 0$ at $\varphi \geq 0$ and $A = e^{2\rho/\varphi} - 2e^{2\rho/\varphi}$ at $\varphi < 0$. At $\rho = 6$ and $\varphi \rightarrow 0$, MM potential is just the LJ potential. And MM

[a)] Author to whom correspondence should be addressed. Electronic mail: clj@ustc.edu. Tel./Fax: +86-551-5107342.

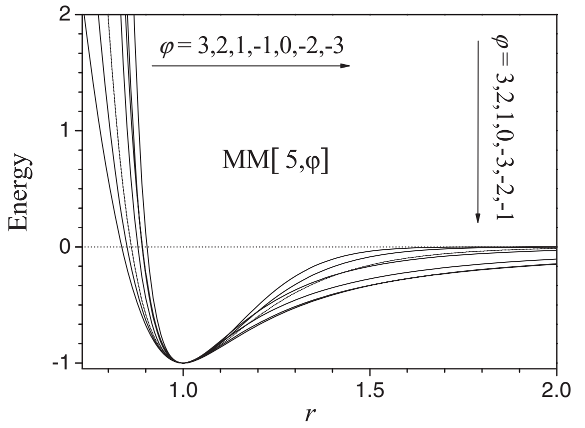

FIG. 1. Plots of the LJ and the MM potential for different values of φ.

potential is the Morse potential at $\varphi = 1$. Figure 1 shows that potentials with similar ranges at the minimum can have various short- and long-range interactions. With φ increasing, the potential range at short range will decrease and the potential range at long range will increase. By the new parameter φ, we can control the long- and short-range interactions separately. A larger φ means softer short-range interaction and weaker long-range interaction, and a smaller φ means harder short-range interaction and stronger long-range interaction. Figure 2 shows that MM potentials with similar long range interactions can be well fitted by different ρ and φ. So the novel MM potential can freely control the interaction at the minimum, short range, and long range of the potential.

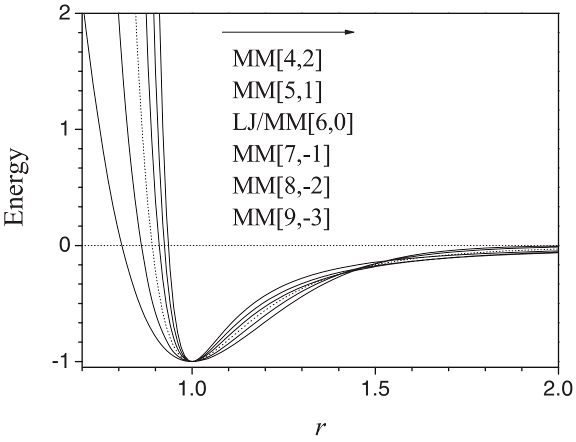

FIG. 2. Plots of MM potentials with similar long range interactions for different ρ and φ.

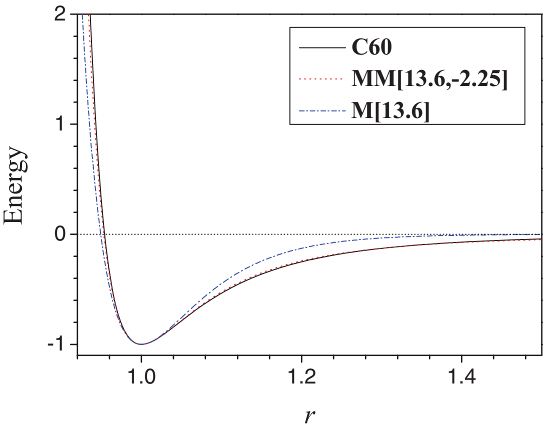

FIG. 3. Plots of Girifalco potential for C_{60}, MM potential for $\rho = 13.6$ and $\varphi = -2.25$ and Morse potential for $\rho = 13.6$. The dotted line is MM potential. The dashed-dotted line is Morse potential. For easy comparison, the Girifalco potential is also plotted in normalized form ($\varepsilon = r_0 = 1$).

Morse potential has been applied to fit the bond and nonbond interactions in a number of empirical potentials.[23–26] For example, the Girifalco potential[27–31] for interactions between C_{60} molecules has same curvature at the minimum ($r = 1$) with Morse potential at $\rho = 13.6$.[32] The difference is that, as shown in Fig. 3, Morse potential is a little softer at the short range ($r < 1$) and much weaker at the long range ($r > 1$). However, using the MM function at $\rho = 13.6$ and $\varphi = -2.25$, MM potential can fit the Girifalco C_{60} potential very well (both at the minimum, long range, and short range). Therefore, we can expect that the MM function can be applied to various systems[33–36] better than Morse function by using the two parameters, and structural phase diagrams of MM potentials may involve certain number of real clusters systems.

B. Global optimization method

Global minimum structures of MM clusters are located by using the funnel hopping[37] method. Funnel hopping contains two levels of local optimization procedures and a global optimization procedure. The first local optimization phase is the limited-memory BFGS (L-BFGS) (Ref. 38) which is a powerful quasi-Newton conjugate gradient method. The second local optimization phase is a cluster surface smoothing method that can locate the minimum of the funnel that contains current structure on PES with low cost. The global optimization phase is a simple version of genetic algorithm.[39–41]

III. RESULTS AND DISCUSSION

To get an understanding of the structures of MM clusters as a function of the range of the potential, for each cluster size among $N = 11$–30, at each pair of ρ and φ (where $\rho = 3.0$, 3.2, 3.5, 4.0, 4.5, 5.0, 6.0, 8.0, 10.0, and 20.0 and $\varphi = -4$, -2, -1, 0, 1, 2, and 4), 5000 iterations of funnel hopping are carried out separately. Then the 5 lowest-energy structures are recorded for each pair of ρ and φ. Finally, for ρ among 3.0–30.0 and φ among -10.0 to 10.0, the global minimum structures at each values of ρ and φ are located from the recorded structures, and the structural phase diagram is plotted which showing how the global minimum structures depend on potential ranges (ρ and φ).

Figures 4–8 plot the resulting structural phase diagrams of $MM_{11–14}$, $MM_{15–18}$, $MM_{19–22}$, $MM_{23–26}$, and $MM_{27–30}$, respectively, where structures of each global minimum labeled by alphabet (i.e. A, B, C, ...) are also listed in the figures. The coordinates of the located global minima can be found in the supplementary material.[42]

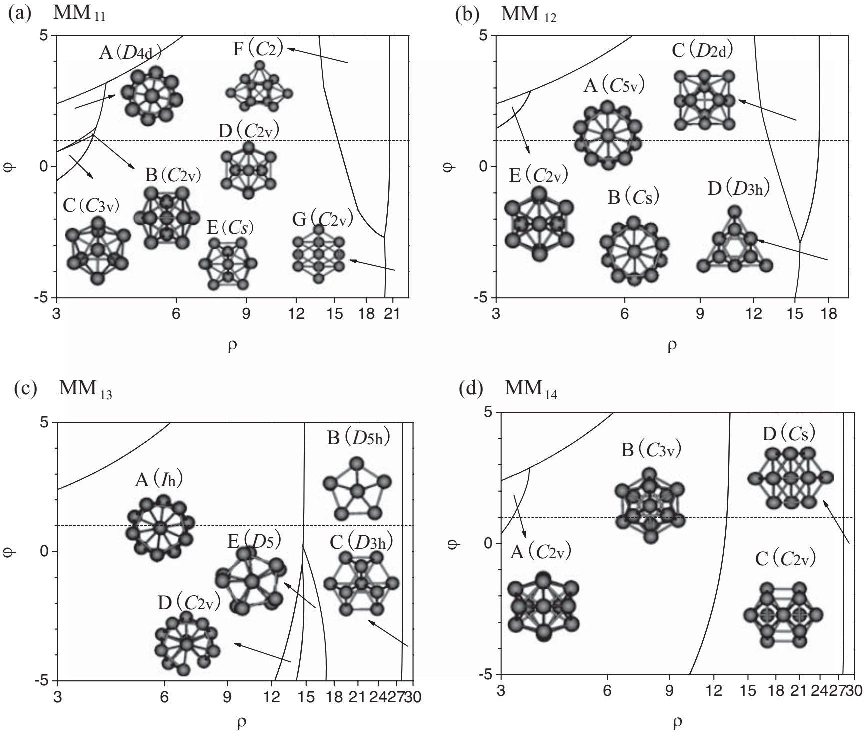

FIG. 4. Structural phase diagrams of (a) MM_{11}, (b), MM_{12}, (c) MM_{13}, and (d) MM_{14} clusters showing the structures of the global minimum depend on ρ and φ. The dashed line gives $\varphi = 1$ which is the Morse potential.

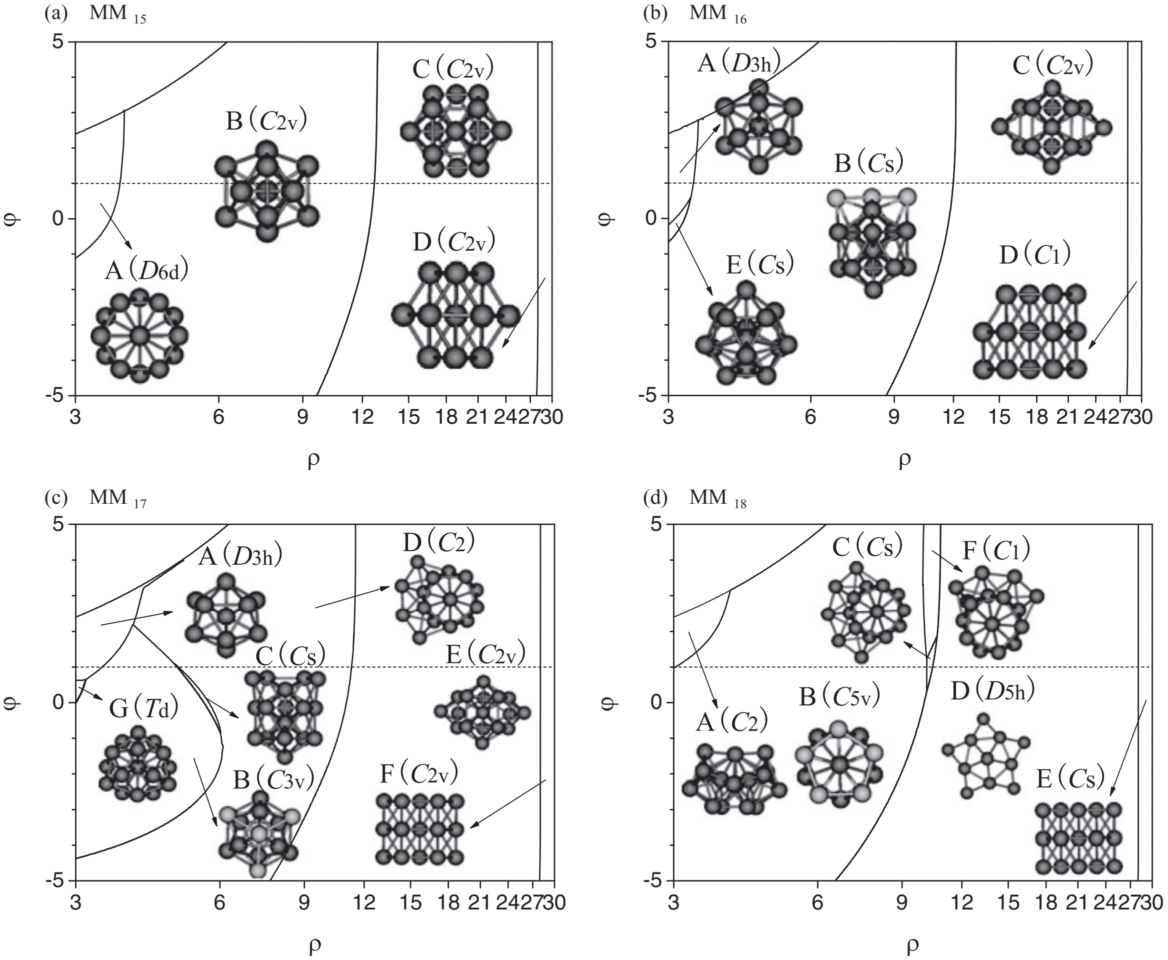

FIG. 5. Structural phase diagrams of (a) MM_{15}, (b), MM_{16}, (c) MM_{17}, and (d) MM_{18} clusters showing the structures of the global minimum depend on ρ and φ. The dashed line gives $\varphi = 1$ which is the Morse potential.

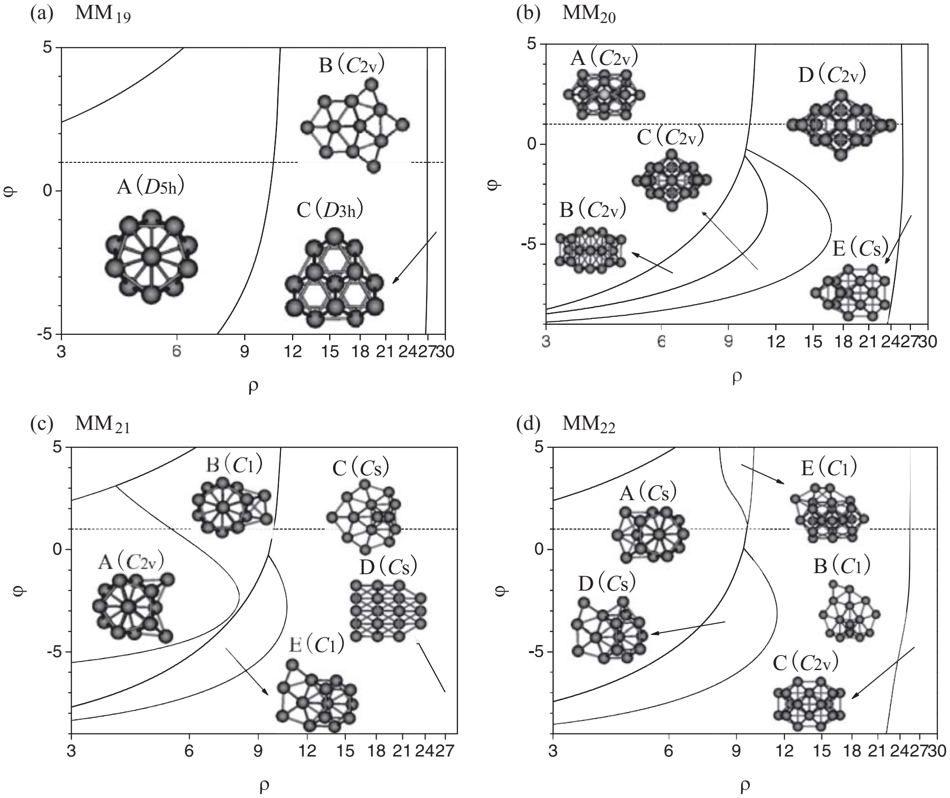

FIG. 6. Structural phase diagrams of (a) MM_{19}, (b) MM_{20}, (c) MM_{21}, and (d) MM_{22} clusters showing the structures of the global minimum depend on ρ and φ. The dashed line gives $\varphi = 1$ which is the Morse potential.

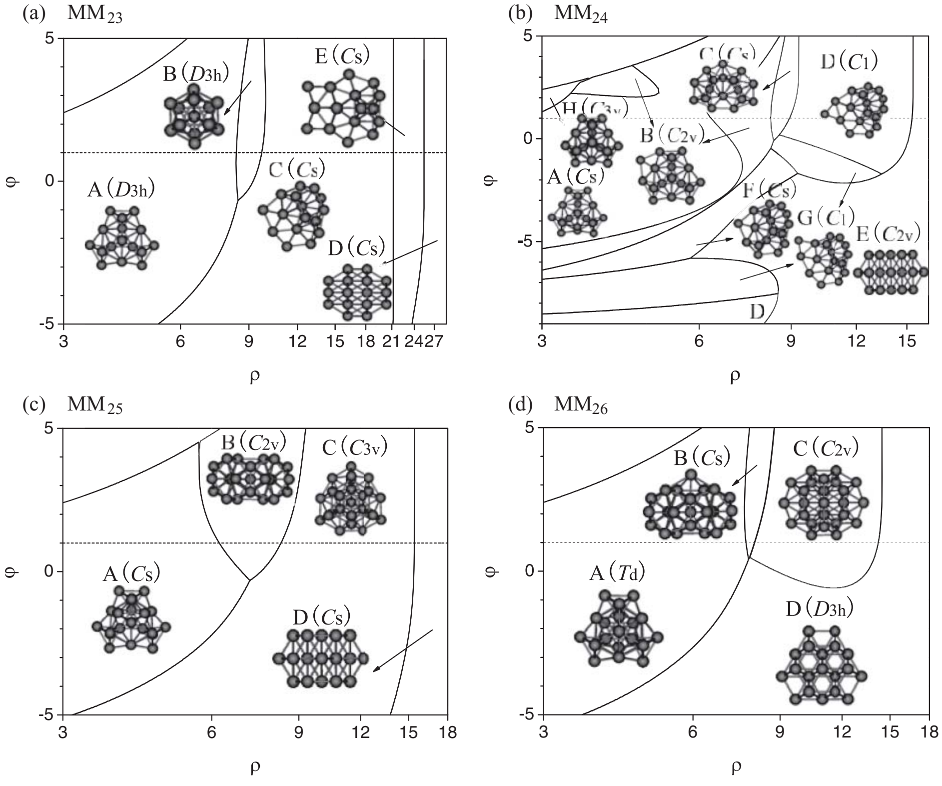

FIG. 7. Structural phase diagrams of (a) MM_{23}, (b) MM_{24}, (c) MM_{25}, and (d) MM_{26} clusters showing the structures of the global minimum depend on ρ and φ. The dashed line gives $\varphi = 1$ which is the Morse potential.

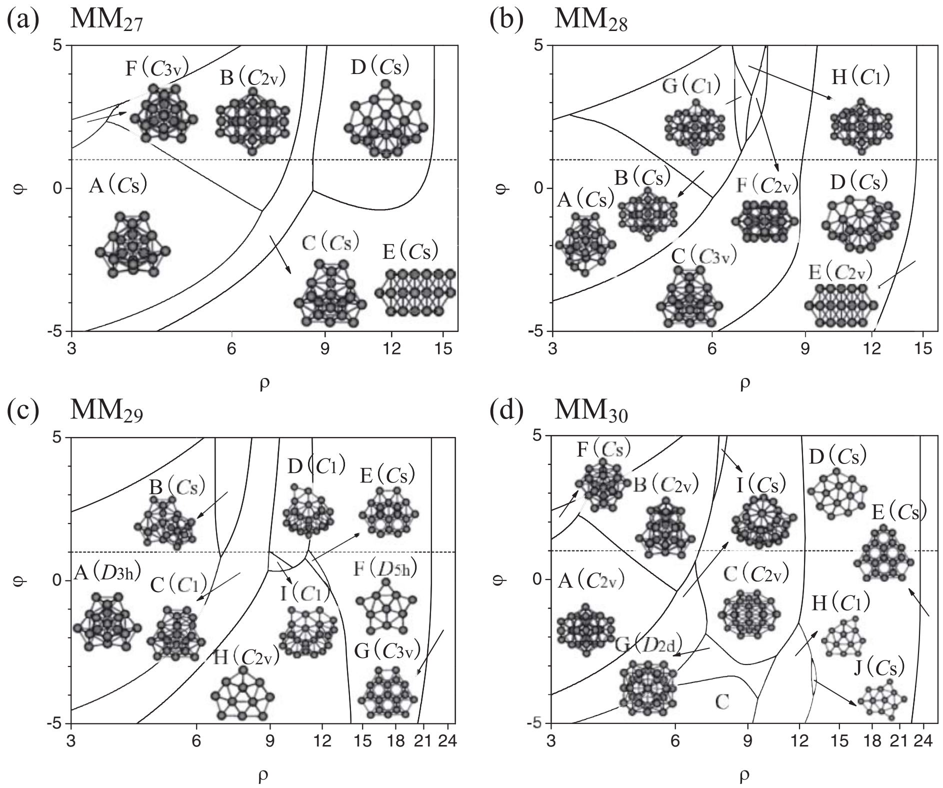

FIG. 8. Structural phase diagrams of (a) MM_{27}, (b), MM_{28}, (c) MM_{29}, and (d) MM_{30} clusters showing the structures of the global minimum depend on ρ and φ. The dashed line gives $\varphi = 1$ which is the Morse potential.

A. Structural phase diagrams of $MM_{11–14}$

As shown in Fig. 4(a), first, at very small values of ρ, the global minima 11A, 11B and 11C are disordered with D_{4d}, C_{2v} and C_{3v} symmetry, respectively, which are spherical but strained. In the three disordered structures, 11A has the largest number of nearest-neighbor contacts (NN), so it is more favored at larger φ; however, 11C is less strained for $r < 1$, so it is more favored at a small φ. Then with ρ increasing, incomplete icosahedra 11D and 11E become more stable because of lower strain energy. 11D is based on the magic number 13-atom icosahedron. 11E has the same structure with 11D, but is little distorted due to the strain and the symmetry is broken (from C_{2v} to C_s), and the transition is smooth without first order phase transition, so it is difficult to find their demarcation line. Next, with ρ increasing or φ decreasing, the strain energy grows so that incomplete icosahedra are destabilized and 11F becomes the global minimum, which is tetrahedral with C_2 symmetry (the packing style is similar to the magic number 98-atom Leary tetrahedron[43]). Lastly, at large values of ρ, 11F also becomes too strained, and the strain free closed-packed 11G (C_{2v}) becomes the global minimum. All these structures are global minima of Morse clusters ($\varphi = 1$) at certain range of the parameter ρ.[19]

Figure 4(b) plots the structural phase diagram of MM_{12}. It can be seen that, at very large area of the diagram, the global minima are icosahedral 12A (C_{5v}) and 12B (C_s), where 12B has same structure with 12A, but is little distorted and the symmetry is broken, and the transition is also smooth without first order phase transition, so it is difficult to find their demarcation line; at large values of ρ and φ, the global minimum 12C is tetrahedral with D_{2d} symmetry (similar to 11F); at very large values of ρ, the global minimum 12D is strain free close packed with D_{3h} symmetry. At small value of ρ and large value of φ, the global minimum 12E is a novel disordered motif with C_{2v} symmetry, which is compact but strained.

Figure 4(c) plots the structural phase diagram of MM_{13}. At very large area of the diagram, the global minimum 13A is the magic number Mackay icosahedron with I_h symmetry; then with ρ increasing, 13A is destabilized because of strain energy, so decahedron 13B (D_{5h}) becomes the global minimum; and finally the global minimum 13C is close packed with D_{3h} symmetry at very large values of ρ. Between the icosahedral (13A) and decahedral (13B) global minima, at negative values of φ, there are two novel distorted global minima 13D and 13E. 13D is a distortion of icosahedral 13A due to the strain, where the symmetry is broken (from I_h to C_{2v}). 13E is a distortion of the decahedral 13B along the five fold axis, and the symmetry is broken to D_5, which is some what the middle point of the decahedral and icosahedral structures.

Figure 4(d) plots the structural phase diagram of MM_{14}. First, at small values of ρ and positive values of φ, the global minimum 14A is disordered with C_{2v} symmetry, which is compact but strained. Then with ρ increasing, the global minima are icosahedral (14B), decahedral (14C), and close packed (14D), respectively. 14B is 13A plus one atom site; 14C is 13B plus one atom site; and 14D is 13C plus one atom site.

B. Structural phase diagrams of $MM_{15–18}$

In this group, MM_{15} has four kinds of structures as shown in Fig. 5(a), in which no new structures are found compared to Morse potential ($\varphi = 1$). 15A is disordered with D_{6d} symmetry at small values of ρ and not too negative values of φ, which is most compact and has the largest number of NN. Then with ρ increasing, 15B that has less NN but is less strained becomes favored, which is 13A plus anti-Mackay layers with C_{2v} symmetry. Decahedral 15C (C_{2v}) is 13B plus two atoms at large ρ. Lastly, at very large values of ρ, 15D is strain free close packed with C_{2v} symmetry.

Figure 5(b) plots the structural phase diagram of MM_{16}. First, at small values of ρ and small positive values of φ, 16A is disordered with D_{3h} symmetry, which is spherical but very strained. Then with ρ increasing, icosahedral 16B (C_s) is 13A plus anti-Mackay layers, which has less NN but is less strained compared to 16A. Then, decahedral 16C (C_{2v}) becomes favored, which is 13B plus three atom sites. Finally, strain free close packed 16D with C_{2v} symmetry becomes dominant at very large values of ρ. However, at very small values of ρ and not too negative values of φ, the global minimum 16E is a novel disordered structure with C_s symmetry.

Figure 5(c) plots the structural phase diagram of MM_{17}. 17A (D_{3h}) is disordered at small values of ρ and positive values of φ, which is most compact and has two center atoms. Then with ρ increasing or φ decreasing, icosahedral 17B (C_{3v}), 17C (C_s), and 17D (C_2) become global minima, which are all 13A plus various anti-Mackay layers. Next, with ρ increasing, decahedral 17E (C_{2v}) becomes global minimum, which is 13B plus four atom sites. Finally, at very large values of ρ, 17F is close packed with C_{2v} symmetry. 17G is a novel disordered structure with T_d symmetry at very small values of ρ and very narrow ranges of φ, which has one center atom and 16 surface atoms.

Figure 5(d) plots the structural phase diagram of MM_{18}. First, 18A is disordered with C_2 symmetry at small values of ρ and positive values of φ. Then with ρ increasing or φ decreasing, 18B, 18C, and 18F are 13A plus various anti-Mackay sites with C_{5v}, C_s, and C_1 symmetry, respectively, in which 18F is a new structure compared to Morse potential. Next, the decahedral 18D becomes more favored with less strained which is 13B plus five atom sites with D_{5h} symmetry at large values of ρ. Lastly, 18E is close packed with C_s symmetry at very large values of ρ.

C. Structural phase diagrams of $MM_{19–22}$

Figure 6(a) plots the structural phase diagram of MM_{19}. There are just three kinds of structures in the phase diagram, where 19A is double interpenetrating icosahedron with D_{5h} symmetry and which is also a most stable magic number of icosahedral clusters; with ρ increasing, decahedral 19B with C_{2v} symmetry becomes the global minimum; and, finally, close-packed 19C (D_{3h}) is favored at very large values of ρ.

Figure 6(b) plots the structural phase diagram of MM_{20}. Icosahedral 20A (C_{2v}) is the magic number 19A plus one anti-Mackay site. Then with ρ increasing or φ decreasing, the decahedral clusters, 20C (C_{2v}) and 20D (C_{2v}), become dominant. 20C has same number of NN with 20D, but is more spherical and more strained, so it is more favored at negative values of φ. Between the icosahedral and decahedral structures, the global minimum 20B (C_{2v}) is a fragment of the 34-atom magic number Leary tetrahedron.[43] 20E is close packed with C_s symmetry at large values of ρ.

Figure 6(c) plots the structural phase diagram of MM_{21}. Icosahedral 21A (C_{2v}) and 21B (C_1) are 19A plus different anti-Mackay sites. Then with ρ increasing, at negative values of φ, the novel tetrahedral packing cluster 21E (C_1) becomes more favored. Next, with ρ increasing, decahedral 21C (C_s) becomes the global minima. Finally, 21D is close packed with C_s symmetry at large values of ρ.

Figure 6(d) plots the structural phase diagram of MM_{22}. Icosahedral 22A (C_s) and 22E (C_1) are both 19A plus different anti-Mackay sites, where 22E is less spherical and less strained compared to 22A, so it is more favored at a positive value of φ. 22B (C_1) and 22D (C_s) are both in tetrahedral packing (22B can also be taken as decahedral plus anti-layers over the {111} faces). 22C is close packed with C_{2v} symmetry at large values of ρ.

D. Structural phase diagrams of $MM_{23–26}$

Figure 7(a) plots the structural phase diagram of MM_{23}. 23A (D_{3h}) is triple interpenetrating icosahedron at small values of ρ, which is also a magic number of icosahedra. 23B is double face-sharing polyicosahedral with D_{3h} symmetry, which is less strained compared to 23A, but is less spherical and has less NN at the same time, so it is favored at large values of φ. With ρ increasing, tetrahedral 23C (C_s) and 23E (C_s) are the global minima, where 23E can also be taken as decahedral plus anti-layers. 23D is close packed with C_s symmetry at large values of ρ. 23E is also a newly located global of Morse clusters at potential range $\rho = (21.2, 25.4)$ compared to previous works.[17–19]

Figure 7(b) plots the structural phase diagram of MM_{24}. 24A (C_s) and 24B (C_{2v}) are 23A plus various anti-Mackay sites. 24H (C_{3v}) is a distortion of 24A, which is more spherical and strained, so it is more favored at not too positive values of φ. 24C is face-sharing polyicosahedral with C_s symmetry. 24D (C_1), 24F (C_s), and 24G (C_1) are both Leary tetrahedral. Lastly, 24E is close packed with C_s symmetry at large values of ρ. The areas of 24D and 24G have been divided into two parts by 24F and 24E.

Figure 7(c) plots the structural phase diagram of MM_{25}. 25A is icosahedral with C_s symmetry. Then, at large values of φ, with ρ increasing, 25B is less strained for $r > 1$ which is polyicosahedral with C_{2v} symmetry. Next, with ρ increasing or φ decreasing, Leary tetrahedral 25C (C_{3v}) becomes predominant. Finally, at very large values of ρ, 25D is close packed with C_s symmetry.

Figure 7(d) plots the structural phase diagram of MM_{26}. 26A is four interpenetrating icosahedra with T_d symmetry which is also a magic number. 26B is polyicosahedral with C_s symmetry at large values of φ. 26C is Leary tetrahedral with C_{2v} symmetry. 26D is a magic number close-packed structure with D_{3h} symmetry.

E. Structural phase diagrams of $MM_{27\text{–}30}$

Figure 8(a) plots the structural phase diagram of MM_{27}. 27A (C_s) is 26A plus one site. The newly located structure 27F (C_{3v}) is a distortion of 27A. 27B is polyicosahedral with C_{2v} symmetry at large φ. With ρ increasing, icosahedral 27C (C_s) becomes the global minimum. Then, at large values of φ, with ρ increasing, Leary tetrahedral 27D (C_s) becomes the global minimum. Finally, 27E is close packed with C_s symmetry at large values of ρ.

Figure 8(b) plots the structural phase diagram of MM_{28}. 28A (C_s), 28B (C_s), 28G (C_1), and 28H (C_1) are icosahedral with various anti-Mackay overlayers. 28F (C_{2v}) is polyicosahedral. 28C (C_{3v}) is icosahedral with Mackay overlayers. With ρ increasing, 28D (C_s) becomes global minimum, which can be taken as incomplete Leary tetrahedron or Mackay icosahedron. 28E is close packed with C_{2v} symmetry at large values of ρ.

Figure 8(c) plots the structural phase diagram of MM_{29}. 29A (C_{3h}) and 29B (C_s) are icosahedral with various anti-Mackay overlayers. 29C (C_1) is icosahedral with Mackay overlayers. 29D (C_1) and 29I (C_1) are Leary tetrahedral. Then with ρ increasing or φ decreasing, decahedral 29E (C_s), 29F (D_{5h}), and 29H (C_{2v}) become the global minima. Finally, at very large values of ρ, 29G is close packed with C_{3v} symmetry.

Figure 8(d) plots the structural phase diagram of MM_{30}. 30A (C_{2v}) and 30B (C_{2v}) are icosahedral with various anti-Mackay overlayers. 30F (C_s) is a distortion of 30A to have more NN. 30C (C_{2v}) and 30I (C_s) are icosahedral with various Mackay overlayers. With φ decreasing, Leary tetrahedral 30G (D_{2d}) symmetry becomes dominant. The area of 30C has been divided into two parts because of the existence of 30G. Then with ρ increasing, decahedral 30D (C_s), 30H (C_1), and 30J (C_s) become predominant, where 30H and 30J are less strained at negative values of φ. Lastly, 30E is close packed with C_s symmetry at very large values of ρ.

IV. CONCLUSION

In conclusion, with the funnel hopping method, we have located the putative global minimum structures of modified Morse clusters for cluster size $11 \leq N \leq 30$, some of which are previously unknown compared to Morse clusters ($\varphi = 1$). And we also give out the phase diagrams at each cluster size for an overall view of how ρ and φ affect the global minimum motifs. Compared to Morse clusters, 25 new structures (12E, 13D, 13E, 16E, 17G, 18F, 20B, 20C, 21E, 22D, 22E, 24F, 24G, 24H, 27F, 28F, 28G, 28H, 29H, 29I, 30F, 30G, 30H, 30I, and 30J) are located, which are global minimum at the potential range $\varphi > 1$ or $\varphi < 1$. Most of the newly located structures are icosahedral or decahedral. However, some of them are unexpected at such a potential range, e.g., 13E is somewhat a middle point of icosahedral and decahedral motifs; 17G is a core-shell cluster, which has one center atom and a sixteen-atom shell. Moreover, a new putative global minimum for Morse clusters is also found (23E at potential range $\rho = 21.2$–25.4).

Similar to Morse clusters, parameter ρ determines the potential range at the minimum of the potential. At small values of ρ, the energetically favored motifs are disordered, and then with ρ increasing, the energetically favored structures are icosahedral with anti-Mackay overlayers, polyicosahedral, icosahedral with Mackay overlayers, Leary tetrahedral, decahedral plus anti-Mackay overlayers, decahedral, and close packed in turn. Moreover, parameter φ determines the potential range at the long- and short-distance, which can also greatly affect the energetically favored motifs. For example, polyicosahedral motifs are more favored at large values of φ; spherical motifs are more favored at negative values of φ and small values of ρ. For various systems (e.g., liquids, metal clusters, and molecular clusters), the interaction mechanisms may be very complicated, but the interactions may be similar to the modified Morse potential at certain values of ρ and φ, for example, Girifalco C_{60} potential for $\rho = 13.6$ and $\varphi = -2.25$. So the modified Morse potential may be helpful to provide interesting results for some systems. Moreover, the structural phase diagrams of the modified Morse clusters can act as a structural bank, and the global minimum motifs can be the starting points of first principle calculations.

ACKNOWLEDGMENTS

This work is financed by the National Natural Science Foundation of China (20903001), and by the 211 Project of Anhui University.

[1] K. Bao, S. Goedecker, K. Koga, F. Lancon, and A. Neelov, Phys. Rev. B **79**, 041405 (2009).
[2] H. Arslan, Int. J. Mod. Phys. C **18**, 1351 (2007).
[3] J. P. K. Doye and D. J. Wales, New J. Chem. **22**, 733 (1998).
[4] J. P. K. Doye and D. J. Wales, Phys. Rev. B **59**, 2292 (1999).
[5] C. Barron, S. Gomez, and D. Romero, Appl. Math. Lett. **10**, 25 (1997).
[6] C. Barron, S. Gomez, D. Romero, and A. Saavedra, Appl. Math. Lett. **12**, 85 (1999).
[7] V. E. Bazterra, O. Ona, M. C. Caputo, M. B. Ferraro, P. Fuentealba, and J. C. Facelli, Phys. Rev. A **69**, 7 (2004).
[8] W. S. Cai, H. Y. Jiang, and X. G. Shao, J. Chem. Inf. Comput. Sci. **42**, 1099 (2002).
[9] Y. L. Cao and Y. S. Wang, Acta Phys.-Chim. Sin. **20**, 785 (2004).
[10] For The Cambridge Cluster Database, D. J. Wales, J. P. K. Doye, A. Dullweber, M. P. Hodges, F. Y. Nakamura, F. Calvo, J. Hernández-Rojas, and T. F. Middleton, see http://www-wales.ch.cam.ac.uk/CCD.html
[11] J. P. K. Doye and D. J. Wales, Chem. Phys. Lett. **262**, 167 (1996).
[12] M. P. Hodges and D. J. Wales, Chem. Phys. Lett. **324**, 279 (2000).
[13] J. E. Lennard-Jones, Proc. R. Soc. London, Ser. A **109**, 584 (1925).
[14] P. M. Morse, Phys. Rev. **34**, 57 (1929).
[15] J. Farges, M. F. d. Feraudy, B. Raoult, and G. Torchet, J. Chem. Phys **78**, 5067 (1983).
[16] J. Farges, M. F. d. Feraudy, B. Raoult, and G. Torchet, Adv. Chem. Phys. **70**, 45 (1988).
[17] J. P. K. Doye, D. J. Wales, and R. S. Berry, J. Chem. Phys. **103**, 4234 (1995).
[18] J. P. K. Doye and D. J. Wales, J. Chem. Soc.-Faraday Trans. **93**, 4233 (1997).
[19] L. J. Cheng and J. L. Yang, J. Phys. Chem. A **111**, 5287 (2007).
[20] Y. Feng, L. Cheng, and H. Liu, J. Phys. Chem. A **113**, 13651 (2009).
[21] L. J. Cheng and J. L. Yang, J. Chem. Phys. **127** (12), 124104 (2007).
[22] In this paper, as a benchmark study, we set the pair well depth as the unit of the energy ($\varepsilon = 1$) and the equilibrium pair distance as the unit of the distance ($r_0 = 1$).

[23] L. A. Girifalco and V. G. Weizer, Phys. Rev **114**, 687 (1959).
[24] R. W. Keyes, J. Chem. Phys **29**, 523 (1958).
[25] R. C. Lincoln, K. M. Koliwad, and P. B. Ghate, Phys. Rev. **157**, 463 (1967).
[26] A. R. Ruffa, Phys. Rev. B **24**, 6915 (1981).
[27] L. A. Girifalco, J. Phys. Chem. **96**, 858 (1992).
[28] D. J. Wales, J. Chem. Soc. Faraday Trans. **90**, 1061 (1994).
[29] D. J. Wales, J. Chem. Phys. **101**, 3750 (1994).
[30] J. P. K. Doye, A. Dullweber, and D. J. Wales, Chem. Phys. Lett. **269**, 408 (1997).
[31] J. P. K. Doye, D. J. Wales, W. Branz, and F. Calvo, Phys. Rev. B **64**, 235409 (2001).
[32] D. J. Wales and J. Uppenbrink, Phys. Rev. B **50**, 12342 (1994).
[33] J. P. K. Doye and D. J. Wales, Science **271**, 484 (1996).
[34] M. A. Miller, J. P. K. Doye, and D. J. Wales, J. Chem. Phys. **110**, 328 (1999).
[35] M. A. Miller, J. P. K. Doye, and D. J. Wales, Phys. Rev. E **60**, 3701 (1999).
[36] D. J. Wales, ChemPhysChem. **11**, 2491 (2010).
[37] L. Cheng, Y. Feng, and J. Yang, J. Chem. Phys. **130**, 214112 (2009).
[38] D. C. Liu and J. Nocedal, Math. Program. **45**, 503 (1989).
[39] D. M. Deaven and K. M. Ho, Phys. Rev. Lett. **75**, 288 (1995).
[40] B. Hartke, J. Comput. Chem. **20**, 1752 (1999).
[41] R. L. Johnston, Dalton Trans. **22**, 4193 (2003).
[42] See supplementary material at http://dx.doi.org/10.1063/1.3582790 for the coordinates and structures of the located global minimum structures of modified Morse potentials.
[43] R. H. Leary and J. P. K. Doye, Phys. Rev. E **60**, R6320 (1999).